

Emergence of growth and dormancy from a kinetic model of the Escherichia coli central carbon metabolism

Yusuke Himeoka

University of Tokyo

Namiko Mitarai (✉ mitarai@nbi.ku.dk)

University of Copenhagen <https://orcid.org/0000-0003-0116-7606>

Article

Keywords:

Posted Date: January 7th, 2022

DOI: <https://doi.org/10.21203/rs.3.rs-1193900/v1>

License:  This work is licensed under a Creative Commons Attribution 4.0 International License.

[Read Full License](#)

Emergence of growth and dormancy from a kinetic model of the *Escherichia coli* central carbon metabolism

Yusuke Himeoka*, Namiko Mitarai†

Abstract

Physiological states of bacterial cells exhibit a wide spectrum of timescale. Under nutrient-rich conditions, most of the cells in an isogenic bacterial population grow at certain rates, while a small subpopulation sometimes stays in a dormant state where the growth rates slow down by orders of magnitude. For revealing the origins of such heterogeneity of timescales, we studied the kinetic model of *Escherichia coli* central carbon metabolism including the dynamics of the energy currency molecules. We found that the model robustly exhibits both the growing- and the dormant state. In order to unveil the mechanism of distinct behaviours, we developed a recursive method to simplify the model without changing the qualitative feature of the dynamics. Analytical and numerical studies of the 2-variable minimal model revealed the necessary conditions for the distinct behaviour, namely, the depletion of energy due to the futile cycle and its non-uniform impact on the kinetics because of the coexistence of the energy currency-coupled and uncoupled reactions as well as branching of the network. The result is consistent with the experimental reports that the dormant cells commonly exhibit low ATP levels, and provides a possible explanation for the appearance of dormant cells that causes antibiotic persistence.

Bacterial growth rates span in a wide range of timescales: *Escherichia coli* cells typically double every 20 minutes under the nutrient-rich conditions, while cells can also exhibit dormancy where the growth of cells almost halts and yet the death is strongly suppressed [1–3]. The transition to the dormant states can either be a stochastic event or a response to hostile environments such as starvation and exposure to antibiotics. This dormancy is a beneficial strategy for surviving the nutrient-poor conditions as it can lower the cell’s nutrient requirements [4]. Also, the dormancy is known as the main cause of bacterial persistence that has a high tolerance to antibiotics, and thus, has been gathering attention from a wide range of fields from microbiology to therapeutic studies [2, 3, 5, 6].

Notable changes in the timescale of cellular physiology are happening in the dormant cells. It has been implied that the dormant cells have a sort of memory capacities: The lag time was shown to depend on the length of time that the cells are starved [7, 8] and the death rates of the starved cells differ depending on the previous culture conditions even though the starvation condition is identical [9]. Given that slow dynamics are vital for storing memories, a drastic change in the timescale of cellular physiology is necessary. Indeed, it was reported that the proteome kept changing at least for 8 hours in the starved *E.coli* cells [10].

How does the transition to the dormancy happen? Experimental studies of *E.coli* have revealed the links between the dormancy and several molecules. Increased alarmone (p)ppGpp modulates bacterial physiology by transcriptional reprogramming and the direct adjustments of the target proteins [11, 12]. One of the alternative sigma factors σ^S activates a number of stress response genes [13, 14]. Toxin-antitoxin modules lead to the growth arrest by inhibiting essential cellular processes, such as DNA replication and protein translation [15].

In contrast to such a "genetically-controlled" view of bacterial dormancy, Kim Lewis and colleagues proposed a different, "low-energy" perspective: Decreases in ATP concentration itself lead to dormancy and persistence. The single-cell level ATP quantification revealed that the cells that survived the ampicillin treatment had significantly lower ATP concentrations prior to the antibiotic exposure [16]. A similar scenario

*Universal Biology Institute, University of Tokyo, 7-3-1 Hongo, Bunkyo-ku, Tokyo, Japan

†The Niels Bohr Institute, University of Copenhagen, Blegdamsvej 17, Copenhagen, 2100, Denmark

was proposed by the group also for the pathogenic bacterium, *Staphylococcus aureus*. They added a sublethal amount of arsenate which decreases cellular ATP concentrations [17] to the culture ahead of the antibiotic treatment. Then, the survival fraction of the cells from the ciprofloxacin exposure considerably increased [18].

Motivated by this low-energy hypothesis [16, 18] and studies reporting other roles of ATP depletion in dormancy [19, 20], we analyze a link between the metabolic dynamics and the growth-dormancy transition using a mathematical model. Here, we note that there is a clear time-scale separation between the metabolic dynamics (\approx seconds [21]) and the modulation of protein levels (\approx hours [22]). Thus, the kinetic model of metabolism without explicit genetic regulations should capture the characteristic nature of the transition if the metabolic dynamics, by itself, triggers the growth-dormancy transition.

Therefore, in the present manuscript, we study the kinetic model of *E.coli* central carbon metabolism with the cofactors such as ATP included as variables. To the best of our knowledge, this is the first kinetic model of *E.coli* metabolism where the dynamics of cofactors are dealt as variables: There are a number of studies of kinetic model of *E.coli* central carbon metabolism [23–38]. However, as far as we know, the dynamics of the cofactors are neglected [23–33], or if included, the relaxation dynamics of the models are not actually computed [34–38]. As the experimental studies suggested [16, 18], ATPs may play a central role in the transition to the dormancy. Thus, the cofactors can be vital components of the model for studying the growth-dormancy transition.

In the following sections, we present that the kinetic model of *E.coli* central carbon metabolism with cofactors robustly exhibits two distinct dynamics: One is reminiscent of the normal growth behaviour and the other is analogous to the dormant dynamics. Then we derive the minimal network showing qualitatively the same dynamics. The analysis of the minimal model reveals two necessary conditions for the emergence of both growth and dormant dynamics, namely, the depletion of energy due to the futile cycle and its non-uniform impact on the kinetics because of the coexistence of the energy currency-coupled and uncoupled reactions as well as branching of the network.

The obtained result implies that the depletion of ATP and ADP itself leads to the slow dynamics of the metabolites’ concentrations. This conclusion is consistent with the ”low-energy” view of the bacterial dormancy presented in [16, 39], and highlights the notable impact of introducing cofactors into models. We also discuss the possible applications of our analysis for the studies of dormancy in other species, based on the minimal network motifs.

Results

Model

In the present manuscript, we study the *E. coli* core network [40] as one of the simplest models of the real metabolic reaction networks. The *E. coli* core model was obtained from BiGG database [41]. The model contains stoichiometry and the reversibility of the reactions. The *E. coli* core model has 52 and 75 intracellular metabolites and reactions, respectively. After an appropriate data curation as described later, we implemented the model by using the ordinary differential equation (ODE) that describes the dynamics of concentrations of metabolites.

We applied several modifications to the model to make it suitable for the ODE implementation. First, small molecules such as O_2 , H_2O , and NH_4 , were not considered as variables but treated as constants under the assumptions that the external concentration of these chemicals are kept constant and uptakes/secretions of them take place quickly. The uptake and secretion pathways of all carbon sources except glucose are removed.

Under the anaerobic conditions, cells transfer the free energy to ATP directly, while under the aerobic conditions, most of the energy transfer takes an indirect form: the energy is first transferred to other chemicals such as NADH and NADPH, and then, the stored energy in NADH, NADPH, and others are used for converting ADP to ATP. The conversion yield of ATP per NADH in the *E. coli* core model is 1.25¹ and NADH/NADPH yield is roughly unity. For introducing the cofactors to the model in a simple manner, we

¹via NADH16, CYTB, and ATPS4r.

89 assume that the energy transfers via NADH and NADPH are sufficiently fast and ATP/NADH(NADPH)
 90 yield as unity. According to these assumptions, we replace NAD(NADP) and NADH(NADPH) with ADP
 91 and ATP, respectively (we discussed the validity of this assumption in the Discussion section and *SI text*
 92 Section.9). Full lists of the chemical components and the reactions are provided in *SI Data.1*.

93 Also, the stoichiometry of the growth reaction was modified. The original *E. coli* core model has the
 94 biomass production reaction leading to the cell growth consisting of 16 substrates and 7 products with non-
 95 integer stoichiometry constants. For the kinetic modeling, such reactions having too many substrates and
 96 products leads to numerical instability and non-integer stoichiometry is unreasonable. Thus, we replaced the
 97 biomass production reaction with a following reaction: (Erythrose 4-phosphate) + (L-Glutamine) + (ATP)
 98 \rightarrow (ADP). This reaction is much simpler than the original one but requires the model to run all the modules
 99 of the metabolic reactions, namely pentose phosphate pathway for Erythrose 4-phosphate (e4p), TCA cycle
 100 for L-Glutamine (gln), and energy generation for ATP. Hereafter, we call this simplified biomass production
 101 reaction as the growth reaction.

102 The resulting model consists of 32 variables and 40 reactions. The final metabolic reaction network is
 103 drawn in Fig. 1. Our model cell takes up the nutrient from the node labeled as "glc" which has a constant
 104 concentration, performs successive conversion of the chemicals with generating energy, and proceeds the
 105 growth reaction.

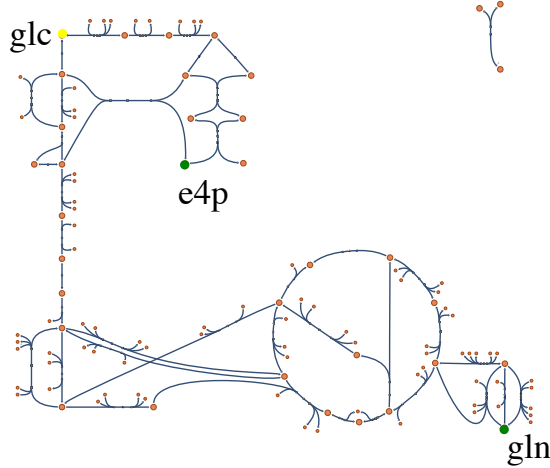


Figure 1: The metabolic network of the *E. coli* core model generated by Escher [41]. The sole carbon source (glucose-6-phosphate) is placed at the left top (abbreviated as glc). We highlighted the substrates of the growth reaction other than ATP, namely, e4p and gln. The growth reaction is not drawn.

106 First, we simulated the model with realistic setups. The kinetic parameters of *E. coli* core model have
 107 been estimated using the metabolic ensemble modeling (MEM) by Khodayari and colleagues [36]. We derived
 108 the Michaelis-Menten type rate equation for each reaction according to the enzyme kinetics used in [36] with
 109 the presented kinetic parameters. Then we assumed that each chemical species is consumed/synthesized by
 110 associated reactions, diluted as the cell grows, and spontaneously degraded at a slow rate. Thus, the temporal
 111 change of the concentration of the i th chemical species X_i is ruled by

$$\frac{d[X_i]}{dt} = \sum_j S_{ij} J_j - d[X_i] - \mu[X_i], \quad (1)$$

112 where S is the stoichiometric matrix and J_i 's are the fluxes due to chemical reactions. d and μ are the
 113 spontaneous degradation rate and the growth rate, respectively. Note that the concentrations of enzymes are
 114 supposed to be constant and lumped in the kinetic parameters. We assumed that spontaneous degradation

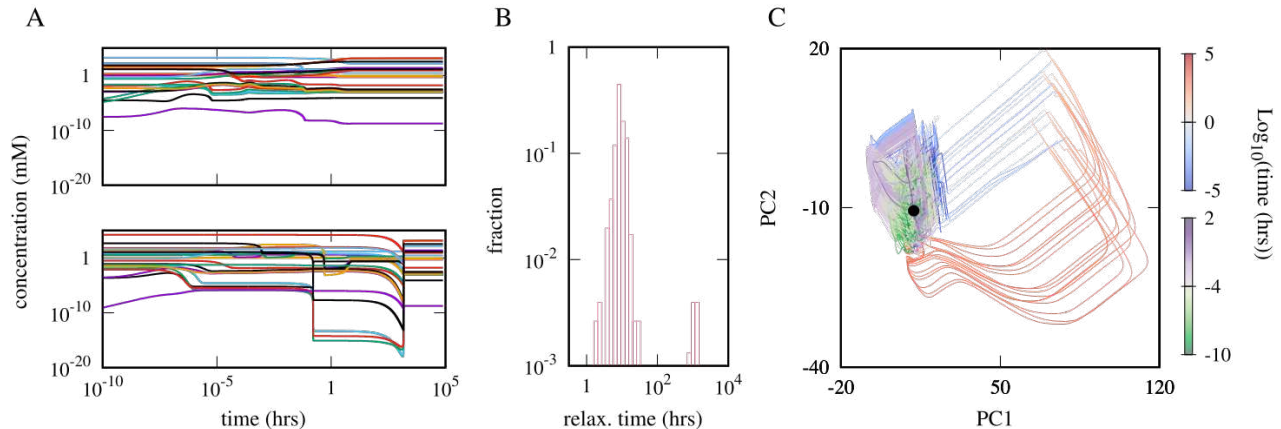


Figure 2: A. Two characteristic dynamics of *E. coli* core model starting from different initial points. While the growth rate of the cell is ≈ 0.5 per hour at the attractor, there are huge differences in the relaxation behaviours between the top and bottom panel. B. The distribution of the relaxation time showing a clear bimodality. C. Trajectories are overlaid in 2-dimensional principal component space. Color indicates \log_{10} of time. The trajectories having shorter relaxation time (several hours) are colored in green-white-purple while the others are colored in blue-white-red. The black point corresponds to the steady-state attractor. Initial concentration of each metabolites is $10^{u_{i,n}} [X_i^{(ss)}]$ (mM) with $[X_i^{(ss)}]$ as the steady-state concentration of the i th metabolite, and $u_{i,n}$ as a random number uniformly distributed in $[-2, 2]$ while the total concentrations of adenine nucleotide carriers are normalized. Parameters other than ones obtained from [36] are $[\text{glc}] = 20(\text{mM})$, $A_t = 1(\text{mM})$, $d = 5 \times 10^{-3}(\text{hour}^{-1})$, $v_g = 3.6 \times 10^4(\text{mM}^{-2} \cdot \text{sec}^{-1})$ and $r = 5.0(\text{mM}^{-1})$.

115 is a very slow process and represented by a single parameter. The dilution and degradation terms are
 116 omitted in the equations of AMP, ADP, and ATP because the de-novo synthesis of the adenine nucleotide
 117 carriers is not modeled in the *E. coli* core model. This assumption is equivalent to suppose the homeostasis
 118 of the total adenine nucleotide carriers. (We check that the assumption can be relaxed by introducing a
 119 phenomenological reaction for the de-novo synthesis of AMP, see *SI Text* Section.8). According to the growth
 120 reaction which we have introduced above, our model cell grows as the reaction (Erythrose 4-phosphate) +
 121 (L-Glutamine) + (ATP) \rightarrow (ADP) proceeds. We chose the simplest kinetics of the growth reaction given
 122 by $J_g = v_g[\text{e4p}][\text{gln}][\text{atp}]$ and the growth rate as $\mu = rJ_g$. We fit the values v_g and r so that the growth
 123 rate at the steady-state is in the range of the typical growth rate of *E. coli* in minimal glucose media, in the
 124 order of 0.1 per hour, and set the spontaneous degradation rate d as approximately one-hundredth of it. The
 125 concentration of the nutrient ($[\text{glc}]$) and the total concentration of the adenine nucleotide carriers (A_t) are
 126 set to 20mM and 1mM, respectively (see *SI Text* Section.1).

127 Dormant trajectory

128 We first computed the steady-state concentrations by simulating the ODE model from random initial condi-
 129 tions. As far as we have checked, there is only a single steady-state. Then, for emulating the exposure to the
 130 sub-lethal stresses which disturb intracellular states, we applied random perturbations to the steady-state
 131 concentration. The initial concentration of each chemical is given by $10^{u_{i,n}} [X_i^{(ss)}]$. Here $[X_i^{(ss)}]$ and $u_{i,n}$
 132 represents the steady-state concentration of the i th metabolite and a random number for the i th metabolite
 133 and n th perturbation sampled from uniform distribution in $[-2, 2]$. The concentrations of ATP, ADP, and
 134 AMP are normalized so that the total concentration is identical for all the initial conditions.

135 We found that the model exhibited two qualitatively distinct relaxation behaviours depending on the

136 initial conditions. The typical time course of each type is plotted in Figs. 2 A in log scale, to depict the
 137 wide range of the concentration and timescale. Even though the two trajectories eventually relax to the
 138 same steady state, the relaxation behaviours are evidently distinct. First, the concentrations after minutes
 139 ($\sim 10^{-1}$ hours) are different between the top and bottom panel in many orders of magnitude². Also, the
 140 characteristic timescale between them is clearly different. The concentrations of the chemicals reach close
 141 to the steady values in minutes in the top panel, while the concentrations keep changing for a much longer
 142 time, $t \approx 10^3$ hours in the bottom panel, which is experimentally indistinguishable from cells stop growing.
 143 When sampled over various initial conditions, the distribution of the relaxation time has a clear bimodality as
 144 shown in Fig. 2B. Here, the relaxation time is defined as the time when the distance between the steady-state
 145 attractor and the state in the logarithm-converted phase space first becomes less than 0.05.

146 For visualizing the differences among the trajectories, we analyzed all the trajectories in the phase space by
 147 the principal component analysis (PCA, see Materials and Methods) where all the trajectories are converted
 148 to the logarithmic scale. We plotted all trajectories projected onto the 2-dimensional principal component
 149 space (PCS) in Fig. 2C. The trajectories were classified into two groups by the relaxation time and differently
 150 colored. The first group is quickly-relaxing trajectories that the trajectory in the top panel of Fig. 2A belongs
 151 to (colored in green-white-purple). The trajectory in the bottom panel of Fig. 2A is grouped into the other
 152 group, colored by blue-white-red which takes a much longer time to relax to the steady-state attractor.

153 The remarkable gaps between the timescale of chemical reactions, and accordingly, the growth rate during
 154 their relaxations highlight the difference between two time courses. The specific growth rate μ at the steady-
 155 state is $\approx 0.5 \text{ hour}^{-1}$ and the model cell achieves this growth rate in a few seconds in the top panel of Figs. 2A,
 156 while less than $10^{-10} \text{ hour}^{-1}$ in the bottom panel at $t = 10^2$ hours (at plateau). Thus, in the following sections,
 157 we call the trajectories of the second group "dormant trajectories" because of their extremely slower growth
 158 rate than that of the other group. Accordingly, the trajectories of the first group are termed "growth
 159 trajectories". The following sections are devoted to unveiling the mechanism leading to the differentiation of
 160 the growth and dormant trajectories.

161 Simplification of reaction kinetics

162 The kinetic *E. coli* core model is, as it is, too complicated to understand the mechanism that leads to the
 163 two distinct relaxation trajectories. Thus, we simplified the *E. coli* core model as follows. First, we modified
 164 the kinetics of the chemical reactions from the Michaelis-Menten formula to the mass-action rate equation.
 165 The rate of the i th chemical reaction $A \rightleftharpoons B$, J_i which was given by

$$J_i = v_i \frac{[A] - k_i[B]}{1 + [A]/K_A^{(i)} + [B]/K_B^{(i)}} \quad (2)$$

166 is replaced by

$$J_i = v_i([A] - k_i[B]), \quad (3)$$

167 where v_i and $v_i k_i$ are the rate constant of forward- and backward reaction, respectively. Note that the mass-
 168 action kinetics (Eq.(3)) is a special form of the Michaelis-Menten kinetics (Eq.(2)) in the parameter region
 169 where $[A] \ll K_A^{(i)}$ and $[B] \ll K_B^{(i)}$ hold (for general arguments, see [42]). The model is then nondimension-
 170 alized by scaling the concentrations by the external glucose concentration and the time by the rate constant
 171 of the glucose uptake. We further simplified the rate equations by setting v_i 's to unity and binarising k_i 's for
 172 all i 's. The *E. coli* core model contains the information of irreversibility for each reaction, and thus, if the
 173 i th reaction is reversible, we set k_i as unity, and otherwise, set it to $\kappa \ll 1$. We term this simplified version
 174 of the kinetic *E. coli* core model as model0 with an index for the following model reduction steps.

175 Surprisingly, the emergence of distinct relaxation trajectories is robust to such an extensive modification
 176 of the model. The qualitative difference of the trajectories (Figs. S1A), bimodality of the distribution of
 177 the relaxation time (Fig. S1B), and the distinction of the trajectories in the PC1-PC2 space (Fig. S1C) were

²The concentrations of several chemicals are smaller than 1 molecule per cell, especially in the bottom panel. We discuss the interpretation later

178 unchanged. This robustness implies that the emergence of the distinct trajectories stems from the structure of
179 the metabolic reaction network of the *E. coli* core model, rather than choices of specific parameter values. We
180 also confirmed that the distinct trajectories emerge if the kinetic parameters are randomly assigned instead
181 of setting them unity (see *SI Text* Section.11).

182 Now it is worth asking, if there are understandably simple, minimal network architecture(s) in the *E. coli*
183 core network which leads to the distinct trajectories. For extracting the architectures, we develop a method
184 of systematic network reduction in the following section.

185 Systematic Model Reduction

186 In the present section, we reduce the *E. coli* core network to obtain a minimal network exhibiting the
187 distinct relaxation dynamics. As far as we know, there is no method to reduce the reaction network without
188 losing the characteristic nature of the relaxation dynamics. Once the concentrations of the cofactors are
189 dealt as variables, metabolic reactions in the model get highly interconnected and the well-known reduction
190 method works poorly. For instance, adiabatic elimination may eliminate merely one or few reactions and it
191 is hopeless to obtain an understandably-simple model. Thus, here we focus only on the emergence of the
192 distinct trajectories. As will be seen, this allows us to derive a much simpler model than the original model.

193 In the following, we remove one or a few reactions from the network step by step and check if the reduced
194 model still exhibits the distinct trajectories (a solid criterion is introduced later). As illustrated in Fig. 3A,
195 we consider two types of reaction removal, namely, the simple removal and the contraction. First, we describe
196 the simple removal. Suppose that there are reactions $A \rightleftharpoons B$, $B \rightleftharpoons C$ and $C \rightleftharpoons A$, and also A and B are
197 connected to the rest part of the network by the other reactions (Fig. 3A-(i)). The simple removal removes
198 the reaction $B \rightleftharpoons C$ and $C \rightleftharpoons A$, and accordingly, eliminate the chemical C because it is a disconnected
199 component in the network.

200 In the contrast, chemical species are merged by the contraction (Fig. 3A-(ii)). It removes a reaction
201 $A \rightleftharpoons E$, and then, the chemical A and E are identified forming a new chemical $\mathcal{A}E$. Here, we avoided the
202 appearance of the dead-end chemical which has only one reaction because networks with dead-end chemicals
203 can cause the heavy accumulation of the chemicals and it potentially leads to an artifactual anomalous
204 relaxation behaviour.

205 At each reduction step, we checked if the reduced model exhibits the two distinct classes of trajectories
206 by computing its dynamics: First, we run the ODE model from 512 randomly generated initial points to
207 search the attractors. Except for a single model, all the intermediate models of the reduction process showed
208 monostability (we will revisit the exception later). Then, 512 initial conditions were generated by perturbing
209 the steady-state concentration in the same way as we did in the previous models.

210 The bimodality of the relaxation time distribution is one of the best intuitive criteria of the distinct
211 trajectories. However, we found in some cases the bimodality was unclear even though there were clearly
212 different types of trajectories when we plotted the time courses and performed PCA. This is because the
213 growth rates during the relaxation of both types of trajectories (growth and dormant) become smaller than the
214 spontaneous degradation rate d , and thus, the relaxation time of all the trajectories becomes approximately
215 $1/d$ ³. Thus, we decided to focus on the similarity of the trajectories instead of the relaxation time itself.
216 Below, we first intuitively explain how we quantify the similarity of the trajectories, and then, introduce the
217 actual measure.

218 Suppose that a model has a single attractor. Then, all the trajectories starting from different initial points
219 eventually converge. We like to categorize the trajectories into different groups in a way that, if a pair of
220 trajectories monotonically approach each other as they converge to the attractor, they belong to the same
221 group. One may naïvely expect that we can state that two trajectories $x(t)$ and $y(t)$ monotonically approach
222 each other if the Euclidean distance between them at the same time point, $d(x(t), y(t))$, is a monotonically
223 decreasing function of t . However, since the initial points are distributed in the phase space, measuring the
224 distance between the points on two trajectories at the same time point is unreasonable.

³In principle, we can overcome this problem by setting d to be sufficiently small such as 10^{-20} . However, it requires ridiculous amounts of computation. The distributions of the relaxation time for all the models in the reduction step are presented in *SI Text* Section.3

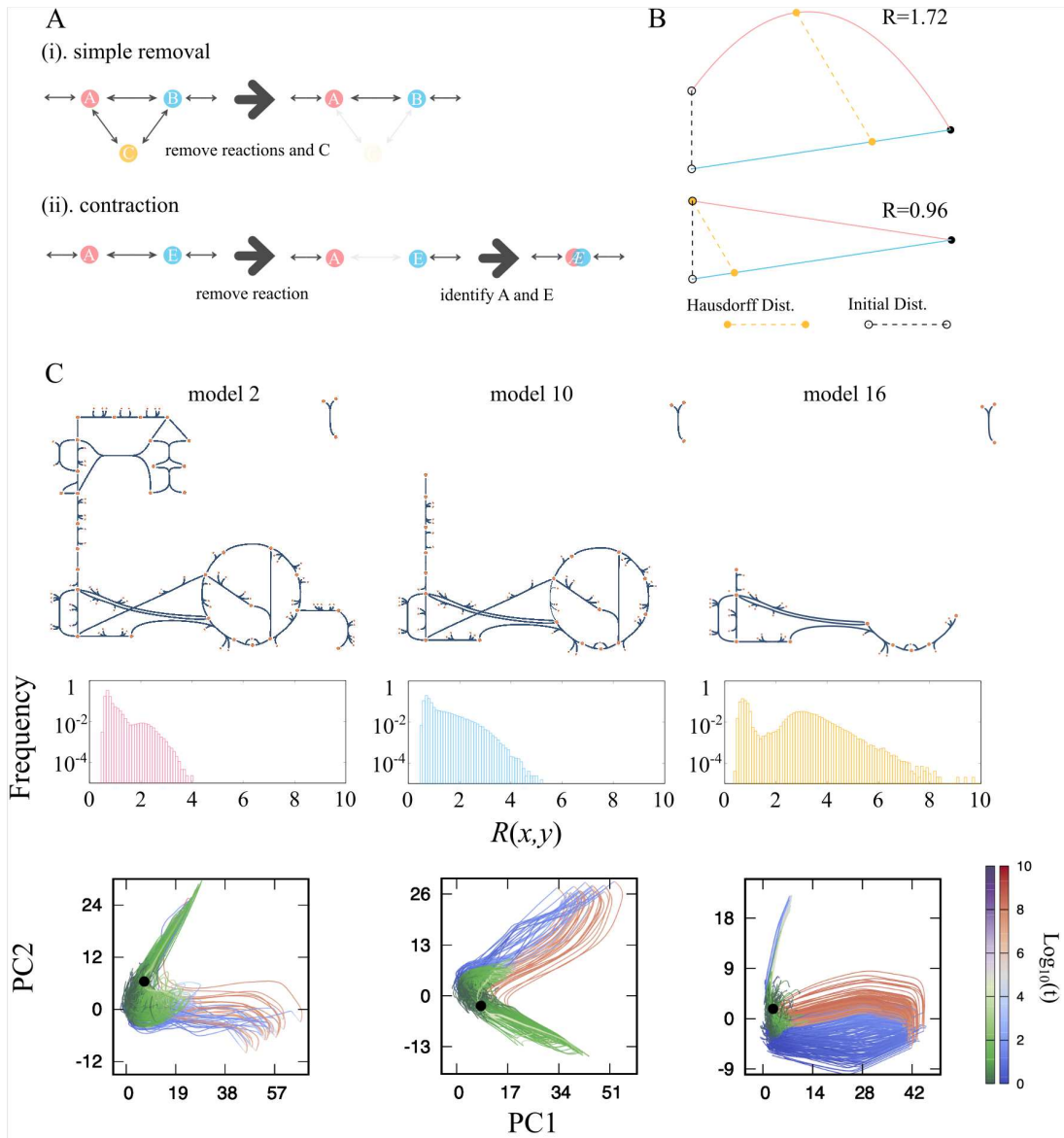


Figure 3: A. Two types of reaction removal. The simple removal (top) just removes one or a few reactions from the network. The number of reactions to be removed is determined so that the dead-end chemicals are not made by the removal. The contraction removes a single reaction first, and then, the substrate and product of the removed reaction are identified and regarded as a new chemical species. B. Illustrative description of the Hausdorff distance and the expansion ratio. There are two cases depicted: the case with $R > 1$ (top) and $R < 1$ (bottom). The two lines (pink and cyan) are trajectories starting from the initial point of each (back circles), converging to the same attractor (black dot). The length of the yellow dashed line and the black dashed line give the Hausdorff distance and the initial distance, respectively. If one trajectory (pink) goes away from the other (blue), typically the Hausdorff distance becomes larger than the initial distance. In the contrast, in the case that the two trajectories approach each other, the Hausdorff distance is smaller than the initial distance. Note that the information of time is discarded in the argument. C. The reduced networks of the intermediate models (models 2, 10, and 16) are drawn. The sole nutrient (glucose) is at the left top corner of the network. The distribution of the expansion ratio and the trajectories projected onto the PCS of each model are also plotted. For the coloring protocol of the trajectories, see the main text.

225 Thus, instead of adopting this naïve definition of the monotonicity, we measure the maximum Euclidean
 226 distance between two trajectories in the phase space. It is known as the Hausdorff distance of the trajectories,
 227 given by

$$d_H(x, y) = \max\{\max_t \min_s d(x(t), y(s)), \max_s \min_t d(x(s), y(t))\}. \quad (4)$$

228 The Hausdorff distance first looks for the closest point of the trajectory y from the point $x(t)$, $y(s^*(t))$, and
 229 then find the pair of the points $(x(t), y(s^*(t)))$ which gives the maximum Euclidean distance. The same
 230 is done from the points of $y(t)$ and the larger value is chosen for the symmetry $d_H(x, y) = d_H(y, x)$. The
 231 Hausdorff distance thus measures how far the two trajectories are distant while trivially distant pairs of
 232 points are not taken into account (for example, the initial point of x and the endpoint of y , i.e, the attractor).

233 We cannot judge whether the trajectories go away from each other or not directly from the Hausdorff
 234 distance since it needs to be compared with the initial separation. Thus, we normalize the Hausdorff distance
 235 by the Euclidean distance between the initial points, $d(x(0), y(0))$ leading to

$$R(x, y) = \frac{d_H(x, y)}{d(x(0), y(0))}. \quad (5)$$

236 We call this ratio $R(x, y)$ as the expansion ratio of the trajectories x and y . It measures how much the initial
 237 distance has expanded. If $d_H(x, y)$ is smaller than the initial distance, $R(x, y)$ is less than unity⁴. $R(x, y) > 1$
 238 means that two trajectories go away from each other at least once despite eventually converging to the same
 239 attractor. The concept of the Hausdorff distance and the expansion ratio are illustrated in Fig. 3B. Note
 240 that in this manuscript, the Euclidean distance, and accordingly, the Hausdorff distance are measured in the
 241 original high-dimensional phase space after applying the logarithm-conversion of the variables, not in the
 242 lower-dimensional principal component space.

243 The distribution is expected to have a trivial peak around $R = 1$. If the distribution has only a trivial peak,
 244 it indicates that all the trajectories are monotonically attracted to a single predominant stream in the phase
 245 space reaching the attractor. Oppositely, if the distribution has a non-trivial peak(s) and/or an additional
 246 long-tail, then it means that the correlation between the initial distance and the Hausdorff distance is not
 247 simply scaled to each other. Therefore, in the present manuscript, we utilize the multimodality and/or the
 248 long-tail of the distribution of the expansion ratio as the criterion of the distinct trajectories (examples can be
 249 found in Fig. 3C). We examine if the model has exhibited distinct trajectories by fitting the distribution by a
 250 sum of Gaussian functions. In rough terms, it checks if the distribution needs at least two Gaussian functions
 251 with distant peaks (see *SI Text* section.2 for the details). Note that in the following analysis, the computation
 252 of the expansion ratio and PCA were performed for the trajectories converted to the logarithmic scale so
 253 that the dynamic behaviours of the chemicals with low concentrations are also reflected in the analysis⁵.

254 A Minimal Model

255 We have reduced the *E. coli* core model step-by-step according to the model reduction method described
 256 in the previous section. For accomplishing the network reduction, we manually determined the order of
 257 the reaction removal so that subsystems of the network are removed or contracted in consecutive reduction
 258 steps. We completed the model reduction by removing and contracting the L-glutamine synthesis pathway (4
 259 steps), pentose-phosphate pathway (4 steps), glycolytic pathway (3 steps), and TCA cycle (7 steps) with the
 260 indicated number of steps in the parenthesis. The full list of the removed reactions is provided in *SI Data.1*.
 261 Also, the distributions of the expansion ratio and the trajectories on PCS of all the models are shown in *SI*
 262 *Text* Section.3. Note that we also tried the model reduction in random orders of the reaction removal (see
 263 *SI Text* Section.10). The minimal networks led by the reduction surely depend on the order of the reaction
 264 removal. However, all the minimal networks commonly satisfied the two conditions for the emergence of the
 265 distinct trajectories discussed later. We revisit the case of random-order reduction in the Discussion section.

⁴ R becomes smaller than 1 if there is any point on x which is closer to $y(0)$ than $x(0)$. This argument is symmetric for the swap of the indices.

⁵As a side effect of the logarithm-conversion, the behaviours of the chemicals with quite low concentrations may be too much highlighted. We computed the expansion ratio with cut-offs of the concentrations for a lower-side, see *SI Text* section.4

266 The reaction network, the distribution of the expansion ratio, and the trajectories projected onto the
267 PCS of selected models are shown in Figs. 3C. The distributions of the expansion ratio show clear bimodality
268 or the long tail. We colored the trajectories based on the relaxation time of each. The figure shows that
269 dormant trajectories (blue-white-red trajectories) commonly take detours to reach the attractor in the PCS.
270 This is not an artifact due to the PCA. We computed the ratio of the line integral of the trajectory (L)
271 to the Euclidean distance between the initial point and the attractor (D) in the original high-dimensional
272 phase space for each trajectory. The average L/D ratio of the dormant trajectories was indeed bigger than
273 that of the growth trajectories (*SI Text* Section.5). We found only the 8th model showed bistability (i.e, two
274 attractors). In the analysis, we chose the major attractor that approximately 92% of the randomly-generated
275 initial points converging. We checked all the initial points generated by the perturbation of this attractor
276 returned back to the attractor. Note that the trajectory starting from perturbed points from the other, minor
277 attractor, also showed a bimodal distribution of the expansion ratio (see *SI Text* Section.6).

278 After the 18 steps of reductions, we reached the stage that no more reduction is possible without losing
279 the multimodality of the distribution of the expansion ratio. The reaction network and reaction names that
280 remained in this minimal network (model 18) are depicted together with the original *E. coli* core network
281 in Fig. 4A. The network consists of glucose (glc), phosphoenolpyruvate (pep), pyruvate (pyr), oxaloacetate
282 (oaa), ATP, ADP, and AMP. As highlighted in the original network, the reaction from glc to pep is the
283 contraction of the glycolytic pathway and oaa is representative of the chemicals in the TCA cycle. It is worth
284 noting that the local structure of the network among pep, pyr, and oaa are unchanged (cyan boxes). In other
285 words, the minimal network is obtained by removing the pentose phosphate pathway and contracting the
286 glycolytic pathway and the TCA cycle. Also, the reaction ADK1 converting two ADPs to ATP and AMP is
287 conserved. As shown in Fig. 4B and C, the model still exhibits distinct trajectories.

288 The model consists of five variables (recall that [glc] and [atp] + [adp] + [amp] are constant). In order
289 to simplify the model further, we adiabatically solved the concentrations of three chemicals, [atp], [adp],
290 and [oaa], under given values of [pep] and [pyr] to eliminate these variables from the model. This adiabatic
291 elimination of the three variables does not violate the multimodality of the distribution of the expansion
292 ratio. The set of ODEs of the minimal model is then given by

$$\begin{aligned}
\frac{d[\text{pep}]}{dt} &= -([\text{atp}][\text{pep}] - [\text{adp}][\text{glc}]) \\
&\quad - ([\text{pep}] - \kappa[\text{oaa}]) + ([\text{atp}][\text{pyr}] - \kappa[\text{amp}][\text{pep}]) \\
&\quad - ([\text{adp}][\text{pep}] - \kappa[\text{atp}][\text{pyr}]) \\
&\quad - (d + r[\text{oaa}][\text{atp}])[\text{pep}], \tag{6}
\end{aligned}$$

$$\begin{aligned}
\frac{d[\text{pyr}]}{dt} &= -([\text{atp}][\text{pyr}] - \kappa[\text{amp}][\text{pep}]) \\
&\quad + ([\text{adp}][\text{pep}] - \kappa[\text{atp}][\text{pyr}]) \\
&\quad - (d + r[\text{oaa}][\text{atp}])[\text{pyr}], \tag{7}
\end{aligned}$$

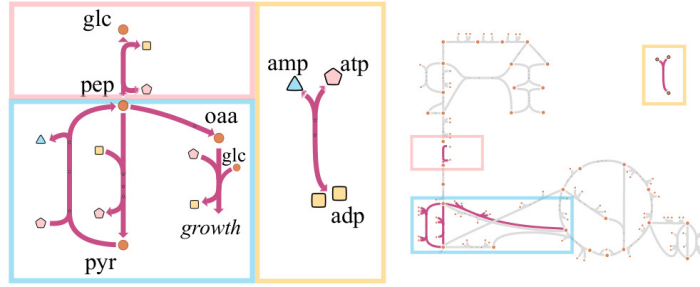
293 where [atp], [adp] (accordingly [amp]), and [oaa] are adiabatically solved, and thus, are the functions of [pep]
294 and [pyr].

295 The two-variable system allows us to visualize the vector field. As shown in Fig. 4D, interestingly, there
296 is a boundary below and above which the streamlines change the direction dramatically ($[\text{pep}] \lesssim 0.1$ and
297 $[\text{pyr}] \approx 1$). Below the boundary, the state relaxes to the attractor rather straightforwardly corresponding to
298 the dynamics shown in Fig. 4B (growth trajectory). On the other hand, trajectories starting from the upper
299 region first travel to the left side of the phase space (small [pep] region) and return back to the attractor,
300 corresponding to Fig. 4C (dormant trajectory). We attribute the emergence of the distinct trajectories to
301 this dramatic change of the directions of the vector field occurring across the boundary. Hereafter, we call
302 the region above- and below the boundary as the dormant and the growth region, respectively.

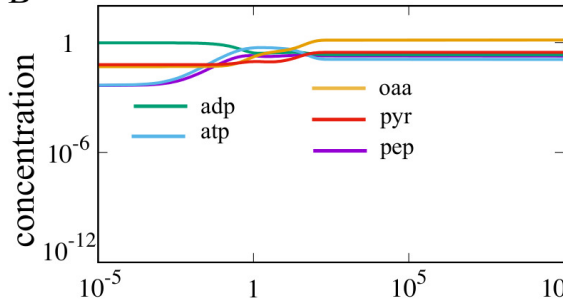
A

Reaction List

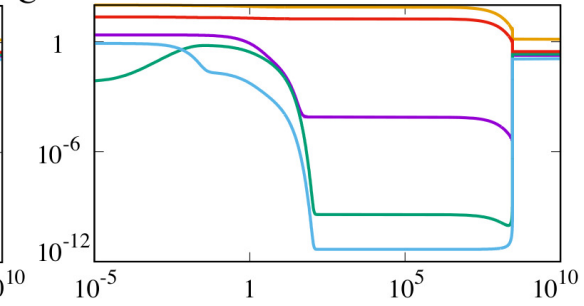
Uptake	$glc + adp \rightleftharpoons pep + atp$
PYK	$pep + adp \rightarrow pyr + atp$
PPS	$pyr + atp \rightarrow pep + amp$
PPC	$pep \rightarrow oaa$
Growth	$oaa + atp \rightarrow adp$
ADK1	$atp + amp \rightleftharpoons 2 adp$



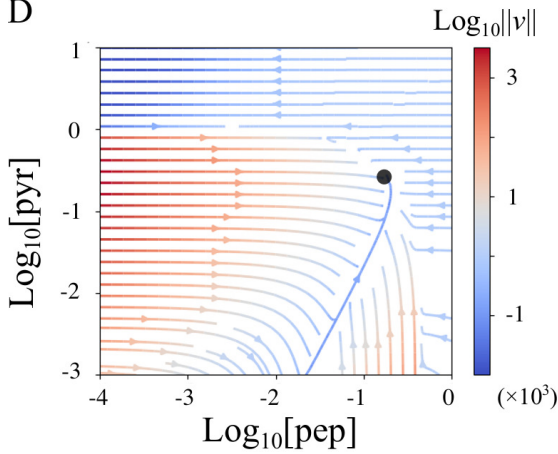
B



C



D



E

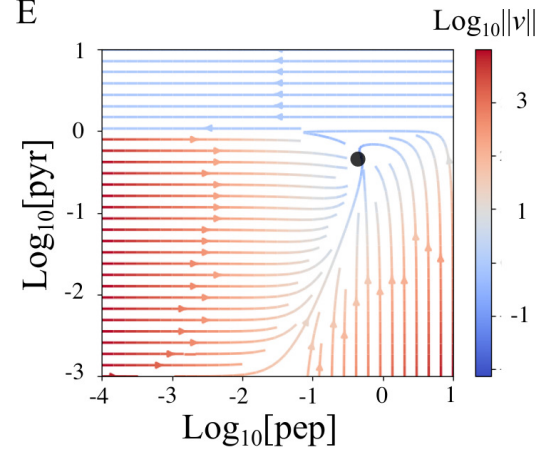


Figure 4: A. The list of the reactions in the minimal network (left). The structure of the minimal network (middle). The original network with the reactions in the minimal model is highlighted (right). The minimal model consists of three parts, namely, the glycolytic pathway (pink bar and boxes), the joint part between the glycolytic pathway and the TCA cycle (cyan bar and boxes), and the adenosine kinase reaction (yellow bar and boxes). B and C. Example time courses of the growth trajectory (B) and the dormant trajectory (C) of the minimal model. D. The streamline representation of the vector field of the 2-variable minimal model where the steady values of $[atp]$, $[adp]$ and $[oaa]$ under given $[pep]$ and $[pyr]$ are numerically solved. E. The streamline representation of the simplified minimal model. The color indicates the norm of the vector $v = (d[pep]/dt, d[pyr]/dt)$ at each point and the black dots indicate the attractor of each in D and E. $\phi_0 = 10^{-8}$ in E.

303 Conditions for the emergence of distinct trajectories

304 What determines the boundary between the growth- and the dormant region, and why is the vector field of
 305 the 2-variable model (Fig. 4D) almost parallel to the horizontal axis in the dormant region? For the first
 306 point, we found that there are large gaps in the concentrations of ATP and ADP between the two regions.
 307 In the dormant region, their concentrations are low ($\sim 10^{-8}$) while in the growth region, they are in the
 308 order of 0.1. This gives an insight into the second point. We found that the drastic change of the direction
 309 of the vector field occurs because four of the five reactions of the model coupled with the adenine nucleotide
 310 carriers, and thus, these reactions almost completely halt in the dormant region.

311 Intuitively, the low level of ATP and ADP in the dormant region can be understood from the reactions
 312 in Fig. 4A as follows. First, let us consider the situation where the concentrations of pep and pyr are in
 313 the dormant region. If in addition, the concentration of pep is low, the uptake reaction proceeds in the
 314 direction $\text{glc} + \text{adp} \rightarrow \text{pep} + \text{atp}$. When this reaction accumulates some ATP, PPS proceeds in the direction
 315 $\text{pyr} + \text{atp} \rightarrow \text{pep} + \text{amp}$, because the concentration of pep is low. In total, the uptake reaction and PPS form
 316 a futile cycle that converts ATP and ADP into AMP. Note that the PPS does not easily result in the
 317 accumulation of pep, because of PPC reaction. If the concentration of pep is high but pyr is also high so that
 318 the system is still in the dormant region, PYK plays the same role as the uptake reaction in the previous
 319 case. Thus, a futile cycle converting ATP and ADP into AMP is formed in both cases. If the conversion
 320 from ATP and ADP into AMP is slow enough, the other reaction, ADK1 ($\text{atp} + \text{amp} \rightleftharpoons 2\text{ADP}$) proceeds to
 321 balance $[\text{atp}] + [\text{adp}]$ and $[\text{amp}]$. However, ADK1 cannot balance them if the conversion is too fast because
 322 the reaction needs ATP.

323 Indeed, this intuitive description is consistent with the analytical estimate of the boundary. For that, we
 324 derive the boundary between the growth and dormant region for $[\text{pep}] \ll 1$. The boundary is given by the
 325 concentration of pyr leading to a low concentration of ATP and ADP with a given value of $[\text{pep}]$. For the
 326 estimation of the critical $[\text{pyr}]$, we sum up $d[\text{atp}]/dt$ and $d[\text{adp}]/dt$ and assume $[\text{atp}], [\text{adp}], [\text{pep}] = O(\epsilon)$ with
 327 $\epsilon \ll 1$. Also, recall that the irreversibility parameter κ in (Eq. (6)) is small. Then we obtain

$$\frac{d([\text{atp}] + [\text{adp}])}{dt} = J_{\text{ADK1}} - J_{\text{PPS}} \sim [\text{atp}](v_{\text{ADK1}}A_t - v_{\text{PPS}}[\text{pyr}]), \quad (8)$$

328 where we explicitly write down the rate parameter v_* 's and the total concentration of adenine nucleotide
 329 carriers A_t for the interpretation of the estimate. If the first term of the right most side is larger than the
 330 second term, $[\text{atp}] + [\text{adp}]$ increases, while in the opposite situation the sum keeps decreasing to zero as long as
 331 $[\text{atp}]$ is non-zero. This shift occurs at $v_{\text{PPS}}[\text{pyr}] \sim v_{\text{ADK1}}A_t$, and it gives the boundary between the growing
 332 and the dormant regions.

333 Next, we explain how the decrease of $[\text{atp}]$ and $[\text{adp}]$ leads to the vector field parallel to the horizontal axis
 334 in the dormant region (Fig. 4D). Let us assume that the concentrations of ATP and ADP are approximately
 335 the same and well-represented by a single lumped parameter ϕ . Also, for a simplicity, we set the irreversibility
 336 parameter κ to zero. Then, the ODE for the 2-variable minimal model (Eq. (6)) is given by

$$\frac{d[\text{pep}]}{dt} = \phi(1 - [\text{pep}] + [\text{pyr}] + r[\text{oaa}]) - (1 + d)[\text{pep}], \quad (9)$$

$$\frac{d[\text{pyr}]}{dt} = \phi([\text{pep}] - [\text{pyr}] + r[\text{oaa}]) - d[\text{pyr}], \quad (10)$$

337 where $[\text{oaa}]$ is the function of ϕ , while it becomes constant as ϕ approaches 0. From the equation, we can see
 338 that if the concentration of ATP and ADP, represented by ϕ , is $O(1)$ (i.e, in the growth region), the timescale
 339 of the system is $O(1)$. On the other hand, if ATP and ADP deplete and $\phi \approx 0$ holds in the dormant region,
 340 the timescale of $d[\text{pyr}]/dt$ becomes $O(d)$. Since the spontaneous degradation rate d is sufficiently smaller
 341 than unity, $|d[\text{pep}]/dt| \gg |d[\text{pyr}]/dt|$ holds, and it leads to the vector field being almost parallel to the $[\text{pep}]$
 342 axis as depicted in Fig. 4D.

343 To confirm if the simplification above still captures the feature of the vector field in Fig. 4D, we have
 344 drawn the vector field of the simplified model Eq.(9) and (10) with $\phi = \max\{1 - [\text{pyr}], \phi_0\}$ in Fig. 4E. It
 345 well captures the feature of the original vector field. We have confirmed that the shape of the vector field is

346 robust to the choice of the function ϕ . Also, we analytically solved the model without the growth dilution
347 term (Eq.(9) and (10) with $r = 0$) and found that the model has only a single timescale which is $O(1)$ in the
348 growth region (see *SI Text* Section.7).

349 The simplified model (Eq.(9) and (10)) highlights that the timescale of $d[\text{pep}]/dt$ is much faster than that
350 of $d[\text{pyr}]/dt$ in the dormant region. The right hand side of Eq.(9) has the term $(1 + d)[\text{pep}]$, while that in
351 Eq.(10) is only the degradation term $d[\text{pyr}]$, and this difference results in the parallel streamline in the phase
352 space (Fig. 4E). It is worth noting where the term $(1 + d)[\text{pep}]$ in Eq.(9) comes from. d corresponds to the
353 constant-rate degradation term, and the reactions coupled with either ATP or ADP should have the rate
354 being proportional to ϕ . Therefore, this timescale 1 comes from the reaction coupled neither with ATP nor
355 ADP, namely, PPC ($\text{pep} \rightarrow \text{oaa}$). All the reactions except PPC are coupled with either ATP or ADP, and
356 thus, the reactions slow down over the boundary between the growth- and the dormant region. However, the
357 rate of PPC has no direct effect from the depletion of ATP and ADP. Then, even after the slowing down of
358 almost all reactions, pep is kept being consumed, and it leads to the characteristic dynamics of the dormant
359 trajectory.

360 Note that, if PPC were also coupled with ATP and ADP, $(1 + d)[\text{pep}]$ term in Eq.(9) would have been
361 replaced by $(\phi + d)[\text{pep}]$. In such a case, all the reactions would have been uniformly slowed down by the
362 depletion of ATP and ADP, and the direction of the vector field would not change over the boundary as
363 drastically as Fig. 4D. Thus, it is vital that the reaction system partially slows down due to the depletion of
364 ATP and ADP.

365 It is noteworthy that the network structure is also a part of the mechanism: if PPC were the reaction
366 converting pyr to oaa instead of pep to oaa, the drastic change of the direction of the vector field as Fig.4D
367 would not result. If PPC were $\text{pyr} \rightarrow \text{oaa}$, the main part of the reaction network (reactions except for ADK1)
368 would have no branch. The slowing down of the upstream reactions of PPC (i.e, uptake, PYK, and PPS)
369 would be rate-limiting steps of it and PPC would slow down coordinated with these reactions.

370 The above two points may suggest that large discrepancies of the chemical concentrations between the
371 steady-state and the plateaux lead to distinct dynamics. In both cases—PPC with energy coupling and the
372 main network without a branch—the reactions uniformly slow down. In such scenarios, even if ATP and ADP
373 deplete, the difference between production and consumption of each chemical stays relatively small, and thus,
374 the changes of the concentrations remain small. However, if the slowing-down occurs heterogeneously on the
375 network, some chemicals will have a large mismatch between production and consumption. As a consequence,
376 the concentrations of such chemicals drastically change from the concentrations before the depletion of ATP
377 and ADP.

378 To sum up, the mechanism of the emergence of the distinct trajectories has two parts: (i) the unbalance
379 of energy (ATP and ADP) production and consumption, and (ii) partial slowing-down of the reaction system
380 caused by non-uniform coupling to the energy currencies and branching of the network.

381 Discussion

382 We have shown that *E.coli* central carbon metabolism exhibits distinctly different dynamics depending on
383 the perturbation from the steady-state concentration. The two types of trajectories greatly differed in terms
384 of the relaxation time and the growth rate during the relaxation, and thus, we termed them as the growth-
385 and the dormant trajectories. We developed a systematic method to simplify the reaction network without
386 losing the distinct trajectories. By the successive reduction of the model, we eventually reached the minimal
387 network still exhibiting the qualitatively same behavior.

388 By drawing the vector field of the 2-variable minimal model, we found that there is a boundary at which
389 the vector field changes the direction drastically. Indeed, the two regions are divided by the boundary
390 corresponding to the set of the initial points of the growth- and the dormant trajectories. The analysis led
391 that there are at least two vital requirements for the distinct trajectories: (i) the unbalance of the energy
392 production and consumption and (ii) the partial slowing-down of the reactions due to the non-uniform
393 coupling with the energy currency molecules and branching of the network.

394 We carefully examined the robustness of our main results, namely, the emergence of distinct trajectories
395 and the consequence of model reduction by studying several model variants. First, the robustness of the emer-

396 gence of distinct trajectories to the parameter values was examined. For several values of the total adenine
 397 nucleotide carriers concentration (A_t), we randomly assigned the rate constant (v_i) and the irreversibility
 398 constant (k_i) of each reaction (Eq.(3)) and studied if the distribution of the expansion ratio is multimodal
 399 and/or long-tailed. As anticipated from the analysis, if the total concentration, A_t , is too large for the depletion
 400 of ATP and ADP to occur, the expansion ratio becomes unimodal (*SI Text* Section.11). Otherwise, the
 401 multimodality was robust to the parameter choice. We confirmed that the model without the replacement of
 402 the nicotinamide nucleotide carriers by the adenine nucleotide carriers exhibits distinct trajectories (*SI text*
 403 Section.9). Also, we have confirmed that the distinct trajectories emerge if the assumption on the constant
 404 total concentration of the adenine nucleotide carriers is relaxed by introducing a phenomenological reaction
 405 for the de-novo synthesis of AMP to the minimal model (*SI Text* Section.8). Overall, the emergence of distinct
 406 trajectories is a robust feature of the *E.coli* core model rather than a phenomenon led by fine-tuning of
 407 the parameters.

408 To confirm if the requirements are not limited to the specific model reduction example, we performed
 409 the reaction removal for the model reduction in 16 different randomized orders. All the minimal networks
 410 obtained by the random reduction were larger than those derived in the result section. Interestingly, we found
 411 that there are differences in the network structure depending on whether the distribution of the expansion
 412 ratio shows the clear multimodality or only the long tail. The minimal models with the clear multimodal
 413 distribution share two features: (a) the models keep ADK1 reaction and AMP⁶, and (b) in each network,
 414 there are both reactions, with- and without the coupling to the energy currency molecules (ATP, ADP, and
 415 AMP) as well as branches. The shared features correspond to the requirements above. However, in the
 416 minimal models with only the long-tail, all the reactions are coupled with the energy-currency molecules,
 417 i.e, the above feature (b) is absent. We also found that the total concentration of ATP and ADP plays a
 418 central role in the emergence of distinct trajectories (see *SI Text* Section.5). Overall, our results shed light on
 419 the impact of the cofactors' role on the dormant transition from the mathematical modeling point-of-view,
 420 supporting the hypothesis presented in [16, 18].

421 The present model showed a possibility that the dormancy transition could be triggered by the metabolic
 422 dynamics itself when the metabolic state is perturbed. Here we succeeded to highlight the role metabolic
 423 dynamics because in the present model we set the enzyme level constant based on the clear time-scale
 424 separation between the metabolic reactions and modulations of the protein level [21, 22]. According to what
 425 the minimal model tells us, the perturbation evokes the futile cycle and leads to the depletion of ATP and
 426 ADP. Here, the sources of the perturbation can be starvation, nutrient shift, exposure to antibiotics, pH
 427 stress, or even stochasticity of the intracellular processes.

428 However, the intracellular states of the dormant cells, in reality, may go beyond what we can depict in
 429 terms of metabolites. For instance, the ATP depletion can lead to the protein aggregation [19, 20]. Also,
 430 disturbances of metabolic states may lead to the stress-response systems being controlled by (p)ppGpp,
 431 toxin-antitoxin modules, and the alternative sigma factor σ^S [10–15]. Therefore, the present result suggest
 432 a mathematical mechanism of the transition to the dormancy, while for developing a mathematical theory
 433 of the cells after the transition, we need to extend the model so that the dynamics of gene expression and
 434 protein concentrations are included. This is one of the reasons why the concentrations of some chemicals
 435 went below a single molecule per cell ($\approx 1\text{nM}$) in the dormant dynamics (Fig.2A). The ATP level actually
 436 depletes also in the real cell during the dormant transition, while too strong depletion like what the present
 437 model exhibited may be prevented by regulations⁷.

438 Note that we can find the counterpart of the reactions in the minimal model in the full *E.coli* metabolic
 439 network, and thus, the dormancy transition demonstrated by the minimal model is verifiable by experiments.
 440 The central part of the mechanism is that PPS and PYK can form the futile cycle and the competition
 441 between PPS and ADK1 on the consumption/production of ATP. Indeed, the experiments showed that one

⁶Note that the model reduction algorithm tried to remove the reaction, while the removal was rejected because the distribution of the expansion ratio of the derived models exhibited neither multimodality nor long-tail.

⁷Also in growth dynamics, the concentration of a chemical species which is one of the growth factors, glutamine, becomes lower than 1nM . We attribute this to the technical reason: the gap in the definition of the growth reaction (the biomass synthesis reaction) between the present model and the model in the paper where the kinetic parameters were estimated [36]. In the model studied in [36], the biomass synthesis reaction was not incorporated into the model. Therefore, glutamine is consumed much faster in the present model than the model for the parameter estimation.

442 can induce the ATP-consuming futile cycle between phosphoenolpyruvate and pyruvate via PYK and PPS by
443 overexpressing the ppsA gene [43, 44]. Taken the experimental reports and the present computational results
444 together, we can hypothesize that the overexpression of the pps gene leads to an increase of the persister
445 fraction because PPS converts ATP to AMP.

446 Lastly, we like to remark that the model reduction method developed in the present manuscript can be
447 applied also to the metabolic models of other organisms. We can find several reactions which potentially
448 form a futile cycle from a variety of species. For instance, each of Acetyl-CoA synthetase (KEGGID:R00235),
449 Phosphoribosylpyrophosphate synthetase (R01049), and Asparagine synthase (R00578) [45] converts ATP to
450 AMP and forms a loop in the metabolic networks. These are the minimum requirements for a reaction to
451 form a futile cycle discussed above. Such reactions are widespread from prokaryotes to eukaryotes, and from
452 unicellular to multicellular organisms. Comprehensive studies of the kinetic models of not only *E. coli* but
453 also other organisms may pave a way for understanding the robust and generic network features leading to
454 the multiple timescales of cellular growth and dormancy.

455 Acknowledgments

456 The authors thank Chikara Furusawa and Sandeep Krishna for the fruitful discussion. This work is supported
457 by the research grant (00028054) from VILLUM FONDEN.

458 Materials and Methods

459 Simulation of ordinary differential equations (ODEs)

460 All the ODE computations were performed by using Matlab (Mathworks) `ode23s` function. For searching
461 attractors, we set $10^{u_{i,n}}$ for the i th metabolite as the n th initial value where $u_{i,n}$ is the random number
462 generated from a uniform distribution in $[-1, 1]$. The steady-state concentration $[X_i^{(ss)}]$ is then obtained,
463 initial concentrations for the main analysis of the dynamics are generated as $10^{u_{i,n}}[X_i^{(ss)}]$ with $u_{i,n}$ is the
464 same random number yet distributed in $[-2, 2]$. The ODEs were computed with two tolerance options
465 (`AbsTol` = 10^{-10} , `RelTol` = 10^{-12}) and (`AbsTol` = 10^{-10} , `RelTol` = 10^{-14}) from exactly the same initial
466 points. After the computation, the trajectories with two different `RelTol` values, but from the same initial
467 point were compared for the quality check of the computation. If the Hausdorff distance of the pair of the
468 trajectories was less than 0.5, the trajectories were considered as correctly computed and the trajectory
469 obtained with `RelTol` = 10^{-14} was used for the further analysis, and otherwise, discarded. The quality check
470 of the computation was performed after the transformation $x(t) \rightarrow \ln(x(t))$ where $x(t)$ is the concentration
471 of the chemicals.

472 Hausdorff distance

473 Hausdorff distance is computed by using the python package `scipy.spatial.distance.directed_hausdorff`
474 as the maximum of two directed Hausdorff distances after the transformation of concentration into the natural
475 logarithm of the concentration.

476 Principal Component Analysis

477 We used the python package `sklearn.decomposition.PCA` [46] without whitening. The whitening leads to
478 only a minor effect on the results. The concentrations of the chemicals were transformed into the natural
479 logarithm of the concentration before the analysis.

References

- 480
- 481 [1] Guennadi Sezonov, Danièle Joseleau-Petit, and Richard d’Ari. Escherichia coli physiology in luria-bertani
482 broth. *Journal of bacteriology*, 189(23):8746–8749, 2007.
- 483 [2] Nathalie Q Balaban, Jack Merrin, Remy Chait, Lukasz Kowalik, and Stanislas Leibler. Bacterial persis-
484 tence as a phenotypic switch. *Science*, 305(5690):1622–1625, 2004.
- 485 [3] Nathalie Q Balaban, Sophie Helaine, Kim Lewis, Martin Ackermann, Bree Aldridge, Dan I Andersson,
486 Mark P Brynildsen, Dirk Bumann, Andrew Camilli, James J Collins, et al. Definitions and guidelines
487 for research on antibiotic persistence. *Nature Reviews Microbiology*, 17(7):441–448, 2019.
- 488 [4] Susanne K Christensen, Marie Mikkelsen, Kim Pedersen, and Kenn Gerdes. Rele, a global inhibitor
489 of translation, is activated during nutritional stress. *Proceedings of the National Academy of Sciences*,
490 98(25):14328–14333, 2001.
- 491 [5] Yusuke Himeoka and Namiko Mitarai. When to wake up? the optimal waking-up strategies for
492 starvation-induced persistence. *PLoS computational biology*, 17(2):e1008655, 2021.
- 493 [6] Mikkel Skjoldan Svenningsen, Sine Lo Svenningsen, Michael Askvad Sørensen, and Namiko Mitarai.
494 Existence of log-phase escherichia coli persists and lasting memory of a starvation pulse. *Life Science*
495 *Alliance*, 5(2), 2022.
- 496 [7] Irit Levin-Reisman, Orit Gefen, Ofer Fridman, Irine Ronin, David Shwa, Hila Sheftel, and Nathalie Q
497 Balaban. Automated imaging with scanlag reveals previously undetectable bacterial growth phenotypes.
498 *Nature Methods*, 7(9):737, 2010.
- 499 [8] Yusuke Himeoka and Kunihiko Kaneko. Theory for transitions between exponential and stationary
500 phases: universal laws for lag time. *Physical Review X*, 7(2):021049, 2017.
- 501 [9] Elena Biselli, Severin Josef Schink, and Ulrich Gerland. Slower growth of escherichia coli leads to longer
502 survival in carbon starvation due to a decrease in the maintenance rate. *Molecular Systems Biology*,
503 16(6):e9478, 2020.
- 504 [10] Jakub Leszek Radzikowski, Silke Vedelaar, David Siegel, Álvaro Dario Ortega, Alexander Schmidt, and
505 Matthias Heinemann. Bacterial persistence is an active σ s stress response to metabolic flux limitation.
506 *Molecular systems biology*, 12(9):882, 2016.
- 507 [11] Dao Nguyen, Amruta Joshi-Datar, Francois Lepine, Elizabeth Bauerle, Oyebode Olakanmi, Karlyn Beer,
508 Geoffrey McKay, Richard Siehnel, James Schafhauser, Yun Wang, Bradley E Britigan, and Pradeep K
509 Singh. Active starvation responses mediate antibiotic tolerance in biofilms and nutrient-limited bacteria.
510 *Science*, 334(6058):982–986, November 2011.
- 511 [12] Vasili Haurlyliuk, Gemma C Atkinson, Katsuhiko S Murakami, Tanel Tenson, and Kenn Gerdes. Recent
512 functional insights into the role of (p)ppgpp in bacterial physiology. *Nat. Rev. Microbiol.*, 13(5):298–309,
513 May 2015.
- 514 [13] Regine Hengge-Aronis. Signal transduction and regulatory mechanisms involved in control of the σ s
515 (rpos) subunit of rna polymerase. *Microbiology and molecular biology reviews*, 66(3):373–395, 2002.
- 516 [14] Rv Lange and Regine Hengge-Aronis. Identification of a central regulator of stationary-phase gene
517 expression in escherichia coli. *Molecular microbiology*, 5(1):49–59, 1991.
- 518 [15] Rebecca Page and Wolfgang Peti. Toxin-antitoxin systems in bacterial growth arrest and persistence.
519 *Nature chemical biology*, 12(4):208–214, 2016.

- 520 [16] Sylvie Manuse, Yue Shan, Silvia J Canas-Duarte, Somenath Bakshi, Wei-Sheng Sun, Hirotada Mori,
521 Johan Paulsson, and Kim Lewis. Bacterial persisters are a stochastically formed subpopulation of low-
522 energy cells. *PLoS biology*, 19(4):e3001194, 2021.
- 523 [17] Susan A Moore, DMe Moennich, and MJ Gresser. Synthesis and hydrolysis of adp-arsenate by beef
524 heart submitochondrial particles. *Journal of Biological Chemistry*, 258(10):6266–6271, 1983.
- 525 [18] Brian P Conlon, Sarah E Rowe, Autumn Brown Gandt, Austin S Nuxoll, Niles P Donegan, Eliza A
526 Zalis, Jeremy Clair, Joshua N Adkins, Ambrose L Cheung, and Kim Lewis. Persister formation in
527 staphylococcus aureus is associated with atp depletion. *Nature microbiology*, 1(5):1–7, 2016.
- 528 [19] Yingying Pu, Yingxing Li, Xin Jin, Tian Tian, Qi Ma, Ziyi Zhao, Ssu-yuan Lin, Zhanghua Chen, Binghui
529 Li, Guang Yao, et al. Atp-dependent dynamic protein aggregation regulates bacterial dormancy depth
530 critical for antibiotic tolerance. *Molecular cell*, 73(1):143–156, 2019.
- 531 [20] Avinash Patel, Liliana Malinovska, Shambaditya Saha, Jie Wang, Simon Alberti, Yamuna Krishnan,
532 and Anthony A Hyman. Atp as a biological hydrotrope. *Science*, 356(6339):753–756, 2017.
- 533 [21] JJ Heijnen. Impact of thermodynamic principles in systems biology. In *Biosystems engineering II*, pages
534 139–162. Springer, 2010.
- 535 [22] Markus Basan, Tomoya Honda, Dimitris Christodoulou, Manuel Hörl, Yu-Fang Chang, Emanuele
536 Leoncini, Avik Mukherjee, Hiroyuki Okano, Brian R Taylor, Josh M Silverman, et al. A universal
537 trade-off between growth and lag in fluctuating environments. *Nature*, 584(7821):470–474, 2020.
- 538 [23] Christophe Chassagnole, Naruemol Noisommit-Rizzi, Joachim W Schmid, Klaus Mauch, and Matthias
539 Reuss. Dynamic modeling of the central carbon metabolism of escherichia coli. *Biotechnology and
540 bioengineering*, 79(1):53–73, 2002.
- 541 [24] Hiroyuki Kurata and Yurie Sugimoto. Improved kinetic model of escherichia coli central carbon
542 metabolism in batch and continuous cultures. *Journal of bioscience and bioengineering*, 125(2):251–
543 257, 2018.
- 544 [25] Tuty Asmawaty Abdul Kadir, Ahmad A Mannan, Andrzej M Kierzek, Johnjoe McFadden, and Kazuyuki
545 Shimizu. Modeling and simulation of the main metabolism in escherichia coli and its several single-gene
546 knockout mutants with experimental verification. *Microbial cell factories*, 9(1):1–21, 2010.
- 547 [26] Yukako Tohsato, Kunihiko Ikuta, Akitaka Shionoya, Yusaku Mazaki, and Masahiro Ito. Parameter
548 optimization and sensitivity analysis for large kinetic models using a real-coded genetic algorithm. *Gene*,
549 518(1):84–90, 2013.
- 550 [27] Oliver Kotte, Judith B Zaugg, and Matthias Heinemann. Bacterial adaptation through distributed
551 sensing of metabolic fluxes. *Molecular systems biology*, 6(1):355, 2010.
- 552 [28] Kirill Peskov, Ekaterina Mogilevskaya, and Oleg Demin. Kinetic modelling of central carbon metabolism
553 in escherichia coli. *The FEBS journal*, 279(18):3374–3385, 2012.
- 554 [29] Ahmad A Mannan, Yoshihiro Toya, Kazuyuki Shimizu, Johnjoe McFadden, Andrzej M Kierzek, and
555 Andrea Rocco. Integrating kinetic model of e. coli with genome scale metabolic fluxes overcomes its
556 open system problem and reveals bistability in central metabolism. *PloS one*, 10(10):e0139507, 2015.
- 557 [30] Jimena Di Maggio, JC Diaz Ricci, and M Soledad Diaz. Global sensitivity analysis in dynamic metabolic
558 networks. *Computers & Chemical Engineering*, 34(5):770–781, 2010.
- 559 [31] Katja Bettenbrock, Sophia Fischer, Andreas Kremling, Knut Jahreis, Thomas Sauter, and Ernst-Dieter
560 Gilles. A quantitative approach to catabolite repression in escherichia coli. *Journal of Biological Chem-
561 istry*, 281(5):2578–2584, 2006.

- 562 [32] Vivek Kumar Singh and Indira Ghosh. Kinetic modeling of tricarboxylic acid cycle and glyoxylate bypass
563 in mycobacterium tuberculosis, and its application to assessment of drug targets. *Theoretical Biology*
564 *and Medical Modelling*, 3(1):1–11, 2006.
- 565 [33] C Juan TORRES, Victoria Guixé, and Jorge Babul. A mutant phosphofructokinase produces a futile
566 cycle during gluconeogenesis in escherichia coli. *Biochemical Journal*, 327(3):675–684, 1997.
- 567 [34] Yikun Tan and James C Liao. Metabolic ensemble modeling for strain engineers. *Biotechnology journal*,
568 7(3):343–353, 2012.
- 569 [35] Linh M Tran, Matthew L Rizk, and James C Liao. Ensemble modeling of metabolic networks. *Biophysical*
570 *journal*, 95(12):5606–5617, 2008.
- 571 [36] Ali Khodayari, Ali R Zomorodi, James C Liao, and Costas D Maranas. A kinetic model of escherichia
572 coli core metabolism satisfying multiple sets of mutant flux data. *Metabolic engineering*, 25:50–62, 2014.
- 573 [37] Ali Khodayari and Costas D Maranas. A genome-scale escherichia coli kinetic metabolic model k-ecoli457
574 satisfying flux data for multiple mutant strains. *Nature communications*, 7(1):1–12, 2016.
- 575 [38] Matthew L Rizk and James C Liao. Ensemble modeling for aromatic production in escherichia coli.
576 *PloS one*, 4(9):e6903, 2009.
- 577 [39] Yue Shan, Autumn Brown Gandt, Sarah E Rowe, Julia P Deisinger, Brian P Conlon, and Kim Lewis.
578 Atp-dependent persister formation in escherichia coli. *MBio*, 8(1), 2017.
- 579 [40] Palsson B Orth J, Fleming R. *Reconstruction and Use of Microbial Metabolic Networks: the Core*
580 *Escherichia coli Metabolic Model as an Educational Guide*. 2010.
- 581 [41] Zachary A King, Andreas Dräger, Ali Ebrahim, Nikolaus Sonnenschein, Nathan E Lewis, and Bernhard O
582 Palsson. Escher: a web application for building, sharing, and embedding data-rich visualizations of
583 biological pathways. *PLoS Comput Biol*, 11(8):e1004321, 2015.
- 584 [42] Athel Cornish-Bowden. *Fundamentals of enzyme kinetics*. John Wiley & Sons, 2013.
- 585 [43] R Patnaik, WD Roof, RF Young, and JC Liao. Stimulation of glucose catabolism in escherichia coli by
586 a potential futile cycle. *Journal of bacteriology*, 174(23):7527–7532, 1992.
- 587 [44] Oliver Hädicke, Katja Bettenbrock, and Steffen Klamt. Enforced atp futile cycling increases specific pro-
588 ductivity and yield of anaerobic lactate production in escherichia coli. *Biotechnology and bioengineering*,
589 112(10):2195–2199, 2015.
- 590 [45] Minoru Kanehisa and Susumu Goto. Kegg: kyoto encyclopedia of genes and genomes. *Nucleic acids*
591 *research*, 28(1):27–30, 2000.
- 592 [46] F. Pedregosa, G. Varoquaux, A. Gramfort, V. Michel, B. Thirion, O. Grisel, M. Blondel, P. Prettenhofer,
593 R. Weiss, V. Dubourg, J. Vanderplas, A. Passos, D. Cournapeau, M. Brucher, M. Perrot, and E. Duch-
594 esnay. Scikit-learn: Machine learning in Python. *Journal of Machine Learning Research*, 12:2825–2830,
595 2011.

Supplementary Files

This is a list of supplementary files associated with this preprint. Click to download.

- [SIDataset.zip](#)
- [SIText.pdf](#)